www.sciencemag.org/content/357/6350/487/suppl/DC1

Supplementary Materials for

Complete measurement of helicity and its dynamics in vortex tubes

Martin W. Scheeler, Wim M. van Rees, Hridesh Kedia, Dustin Kleckner, William T. M. Irvine*

*Corresponding author. Email: wtmirvine@uchicago.edu

Published 4 August 2017, *Science* **357**, 487 (2017)
DOI: 10.1126/science.aam6897

This PDF file includes:

Materials and Methods
Supplementary Text
Figs. S1 to S13
Captions for Movies S1 to S7
References

Other Supplementary Material for this manuscript includes the following:
(available at www.sciencemag.org/content/357/6350/487/suppl/DC1)

Movies S1 to S7

Materials and Methods

Hydrofoil Shapes and Specifications

We followed the procedures outlined in (*38*) for generating hydrofoil meshes. All hydrofoils used in our experiments were fabricated using a Connex350 three-dimensional printer and are made of UV cured resin (VeroWhite FullCure835). The hydrofoil trailing edges for the ring and helically wound loops are given by

$$\vec{X}_{ring} = (R_r \cos(\phi), R_r \sin(\phi), 0) \tag{1}$$

and

$$\vec{X}_{helix} = ((R_h + A\cos(n\phi))\cos(\phi), (R_h + A\cos(n\phi))\sin(\phi), -A\sin(n\phi)), \tag{2}$$

where R_r and R_h are the mean radii of the ring and helix respectively, while A and n are the amplitude and mode of the helical winding (Fig. S1A). Values for the particular parameters used in the experiments are listed in the table contained in Figure S1.

Each hydrofoil has the same cross-section regardless of its overall geometry (Fig. S1B). In every case, the chord, or the distance from tip to tail along the center-line of the wing cross-section, is $Ch = 15mm$; the bend, or the angle made by the tangent to the trailing edge and the direction of acceleration, is $\theta_b = 35°$; the leading and trailing edge thicknesses are $t_1 = 3.125mm$ and $t_2 = 0.188mm$ respectively.

Measuring Circulation via PIV

The circulation of each vortex was inferred from a calibration curve obtained by performing a series of independent circulation measurements on vortices produced by the same hydrofoils used in the experimental trials.

The water was first seeded with neutrally buoyant Polyamide Nylon tracer particles with a mean size of $\sim 350\mu m$. The particles were illuminated using a stationary laser sheet, and their motion was captured using a Phantom v1610 fast camera recording at $8000fps$ with a spatial resolution of 768x768 and a scale of $0.188mm/px$. The resulting image stacks were then processed in MATLAB using PIVLab software developed by Thielicke et al. (*39*), resulting in a time series of 2D cross-sectional velocity profiles. Integrating the flow field along contours of sufficiently large radii centered on the vortex provides a measure of the circulation that is both insensitive to the contour radius and immune to potential errors in the PIV reported velocities induced by the high-shear regions near the core (Figs. S2, A and B).

The circulation was measured over a period comparable to the experiment duration, during which it remains constant (Fig. S2C). For each trial, the final velocity of the hydrofoil was measured using an optical encoder. Together, these measurements provide data points for the speed-circulation calibration curve (Fig. S2D). Circulations for any experimental trial were inferred based on the final hydrofoil speed using the calibration curve for that hydrofoil.

Tracer Identification, Tracking, and Analysis Protocol

For each experimental volume, the center-line path is traced using a combination of ridge-extraction (*45*) and fast-marching (*46*) methods, as outlined in (*15*). Once the paths have been identified, any small scale artifacts from the tracing are removed by application of a sinc filter with a cut-off wavelength of $\lambda_c \sim 14mm$ (Figs. S3, A and B). In order to identify the dye particles at each time step, the center-line path is used to isolate a region of the volume centered around the vortex with a square cross-section of edge length $2d \sim 1.2mm$ (shown projected along a transverse direction in Fig. S3C). The volume is then collapsed along the transverse dimensions to produce a 1D intensity profile (Fig. S3D). The locations of the peaks are identified along the center-line path and mapped back to the coordinates of the volume. Once identified, the particles are then tracked in 3D over the course of the experiment using `trackpy` (*47*).

The dimensionless helicity density $\vec{u} \cdot \hat{t}/\Gamma$ of each blob is then calculated at each point in time by taking the dot product of the velocity and tangent vectors at that point and normalizing by the circulation, Γ. This density is then smoothed by convolution with a Gaussian of standard deviation $\sigma_s = 8ms$ (a single time step between experimental acquisitions, Fig. S3F). The contributions from all blobs at a single time are multiplied by their segment length and then summed to produce the total helicity of the vortex loop at that point in time.

Simulation Specifications

For all simulation of vortex columns, we evolve the viscous incompressible 3D Navier-Stokes equations in vorticity-velocity form using a remeshed vortex method (*48–51*). The boundary conditions are periodic along the axis of the vortex tube, and unbounded in the two orthogonal directions (*52, 53*) to avoid undesired effects from periodic images. We enforce the boundary conditions when inverting the Poisson equation for the velocity field, using the high-performance Parallel Fast Fourier Transform library PFFT (*54*). The spatial derivatives are computed using fourth order finite difference schemes, the particle-mesh interpolation is performed with the fourth order M_6^* scheme (*51*), and we use a fourth order accurate Runge-Kutta scheme to advance in time. The simulations of writhing tubes are done with 512^3 resolution, whereas for straight tubes we use 256^3 computational elements. The time step is always dictated by setting the Lagrangian CFL to 0.125 (*49, 51*).

Supplementary Text

Writhe and Parallel Transport

The natural connection between the writhe and the parallel transport framing can be understood by considering a ribbon (Fig. S4). The tangent, $\hat{t}$, of the ribbon center-line and the ribbon's surface together define a basis vector triad $(\hat{t}, \hat{u}, \hat{v})$ at each point along the center-line. The vector $\vec{u}$ points from the center-line to the edge of the ribbon and is normal to the center-line. The remaining unit vector $\hat{v} = \hat{t} \times \hat{u}$ is perpendicular to the surface of the ribbon. If the ribbon is everywhere untwisted, that is, if $\hat{t} \cdot (\hat{u} \times \partial_s \hat{u}) = 0$ at each point on the center-line, then this basis vector triad corresponds to a parallel transport framing for the center-line.

Now if we consider a ribbon that is untwisted, i.e. follows the parallel transport framing, and coils as it moves through space, the ribbon will, in general, not close when it returns to its point of origin. This fact is illustrated by our example ribbon (Fig. S4), whose helical writhing causes the ribbon to wind beyond its starting orientation. This failure to close evidences that even in the absence of twisting, the edges of a ribbon (or the filaments of a bundle) can still wind around each other if the center-line writhes in space.

This winding induced by locally parallel filaments can be equated to the writhe via the Călugăreanu-White-Fuller theorem for ribbons (*55–57*). The theorem states that the number of times the edges of the ribbon are linked Lk_{edges} is the sum of the twist $Tw = \oint \hat{t} \cdot (\hat{u} \times \partial_s \hat{u})\, ds$ of the ribbon and the writhe Wr of the ribbon center-line, or

$$Lk_{edges} = Tw + Wr \Rightarrow Wr = Lk_{edges} - Tw. \tag{3}$$

Note that Lk_{edges}, the linking between the two lines following each edge of the ribbon, is distinct from the linking between two curves Lk discussed in the main text in that it can be well defined for a single curve in space once that curve has been equipped with a ribbon surface. For our example ribbon, we know that $Tw = 0$ since it is everywhere untwisted; however, the linking between the edges of the ribbon Lk_{edges} is not well defined since the ribbon does not close and is instead rotated $\Delta\theta$ beyond its initial orientation. To close the ribbon, we can add an amount of twist equal to $-\Delta\theta/2\pi$, which will then cause the ribbon to close and the edges to become singly linked, i.e. $Lk_{edges} \to 1$. The writhe of the curve, which, as a property of the center-line alone, is unchanged by the addition of this local twist, is given by

$$Wr = 1 + \frac{\Delta\theta}{2\pi} = 1.25 \tag{4}$$

from which, we see that the writhe is measuring the number of complete windings

(Lk_{edges}) plus the partial winding $(\Delta\theta/2\pi)$ present in a ribbon as it follows a parallel transport framing through space.

Calculation of Total Helicity

Our derivation and discussion here of Equation 2 in the main text builds on work conducted by Berger and Field (*34*), and Chui and Moffatt (*58*), and follows closely the treatment of helicity calculations therein. We reproduce much of the discussion here for the reader's benefit, providing an alternative expression for the final result.

Consider a flow in which the vorticity is confined to compact vortex tubes, e.g. Figure 1A in the main text. Inside the vortex tube, we will assume that the vorticity lies on vortex surfaces which are nested tori that fill the entire vortex tube. This assumption is characteristic of flows in which the vorticity is confined to thin tubes. We can label each of these surfaces with a continuous parameter $\chi \in [0, 1]$, where $\chi = 1$ is the outer most vortex surface (the vortex tube) and $\chi = 0$ is the vortex center-line.

Inside the vortex tube, we can define a coordinate system given by (s, r, ϕ), where s is the distance along the center-line, and r and ϕ are polar coordinates that locate points in the plane normal to that center-line. We will assume that our vortex surfaces do not intersect, such that at every point in the tube

$$r\kappa(s) < 1, \tag{5}$$

where $\kappa(s)$ is the local curvature of the center-line at a given arc length s. Since each point is associated with a single vortex surface, we have

$$\chi = \chi(s, r, \phi). \tag{6}$$

If the vortex surfaces do not fold back on themselves, there is then a one-to-one mapping between χ and r, such that we can invert them uniquely, giving

$$r = R(s, \chi, \phi), \tag{7}$$

which allows us to adopt a new coordinate system (s, χ, ϕ) in which the vortex surface label is now a coordinate. This is useful since the vortex lines lie on surfaces of constant χ, such that $\vec{\omega} \cdot \vec{\nabla}\chi = 0$, allowing us to write

$$\vec{\omega} = \omega_1 \hat{e}_1 + \omega_3 \hat{e}_3, \tag{8}$$

where $\hat{e}_i$ are the basis vectors for the (s, χ, ϕ) coordinate system.

The two components that remain in this representation correspond to vortex lines running parallel to the center-line ($\hat{e}_1$, toroidal lines) and vortex lines winding around the center-line ($\hat{e}_3$, poloidal lines). If we consider the field-lines contained inside a particular surface χ, their toroidal components will all pierce a normal cross-section of the vortex surface, producing a toroidal flux $T(\chi)$. Likewise, the poloidal components of the field-lines inside χ will produce a poloidal flux $P(\chi)$ as they pierce the Seifert surface bounded by the center-line. Each of these surfaces is illustrated in Figure S5. It will also be useful to define the complement of the poloidal flux $\tilde{P}(\chi) = P(1) - P(\chi)$, which is the poloidal flux due to field-lines on the surfaces outside of χ.

The toroidal and poloidal fluxes can be related to the total helicity of the vortex tube. Recall that the helicity measures the amount vortex field-lines wind around each other inside the tube. Now we consider an annulus centered about a particular vortex surface χ. The field lines in this thin annulus will in general have both toroidal and poloidal components. The poloidal component contributes to the helicity by winding around the toroidal field-lines threading the cavity of the annulus. The toroidal component inside the annulus also contributes to the helicity by threading the poloidal components of the field-lines living on all the surfaces exterior to the annulus. The total helicity content of the annulus is then the sum of these terms:

$$d\mathcal{H} = \tilde{P}dT - Td\tilde{P}, \tag{9}$$

and the total helicity of the tube is

$$\mathcal{H} = \int_{\chi=0}^{\chi=1} \tilde{P}dT - Td\tilde{P}. \tag{10}$$

Integrating by parts, we can write this as

$$\mathcal{H} = \tilde{P}(\chi)T(\chi)|_{\chi=0}^{\chi=1} - 2\int_{\chi=0}^{\chi=1} T d\tilde{P}, \tag{11}$$

but since $T(0) = 0$ and $\tilde{P}(1) = 0$, the first term vanishes. To perform the remaining integral, we assume that the relationship between toroidal and poloidal fluxes remains the same for all surfaces, that is, $P(\chi) = hT(\chi)$, where $h = const$. This condition, known as the "uniform twist" assumption, corresponds to a state where field-lines on all vortex surfaces have the same total winding around the center-line. In this case, $d\tilde{P} = -hdT$. Plugging this in, we find

$$\mathcal{H} = hT(1)^2 = T(1)P(1). \tag{12}$$

Now we note that $T(1) = \Gamma$, the circulation of the vortex tube. Finally, we can relate the vorticity flux through the Seifert surface to the circulation computed along the boundary of that surface. Since that boundary is the center-line, we see that

$$P(1) = \int \vec{\omega} \cdot \hat{n}\, dA = \oint_C \vec{u} \cdot \vec{d\ell}. \tag{13}$$

Using this condition, we find:

$$\mathcal{H} = \Gamma \oint_C \vec{u} \cdot \vec{d\ell}. \tag{14}$$

This result generalizes to collections of multiple tubes, since the linking between the tubes adds to the vorticity flux through the Seifert surface of each tube, contributing to the path integral. Thus the helicity of such a collection is simply

$$\mathcal{H} = \sum_i \Gamma_i \oint_{C_i} \vec{u} \cdot \vec{d\ell}. \tag{15}$$

Examination of Uniform Twist Assumption

As outlined in the supplementary text section headed Calculation of Total Helicity, two assumptions are required for accurate calculation of the total helicity via Equation 2 in the main text: first, that the vortex satisfies the “uniform twist” assumption ($P(\chi) = hT(\chi)$); and second, that the tubes are sufficiently thin ($a\kappa \ll 1$). Here we examine the first of these assumptions, leaving the second for the following section.

The “uniform twist” assumption ensures that the amount any field-line winds around the center-line is the same regardless of which vortex surface it lives on. While it is not possible to probe vortex surface structure experimentally, we show here that for viscous straight-line vortices this “uniform twist” state is indeed the state that generic non-uniform twist states are attracted to as they evolve.

Consider a straight line vortex, whose vorticity satisfies

$$\vec{\omega}(r,t) = \omega_z(r,t)\hat{z} + \omega_\phi(r,t)\hat{\phi} \tag{16}$$

such that there is no ϕ or z dependence, and no radial component of the vorticity. In this case, the stretching and advection terms in the vorticity equation of motion cancel exactly, leaving

$$\frac{\partial \vec{\omega}}{\partial t} = \nu \nabla^2 \vec{\omega}, \tag{17}$$

which is a diffusion equation for the vorticity. To understand how this equation evolves the twist of the vortex tube, we can rewrite the vorticity with the same degree of generality to now explicitly contain $\tau(r,t)$, the linear twist density of the tube:

$$\vec{\omega} = \Omega(r,t)\left(\hat{z} + r\tau(r,t)\hat{\phi}\right), \tag{18}$$

Note that $\tau(r,t) = \tau(t)$ corresponds to a “uniformly twisted” state, where

$$Tw = \frac{1}{2\pi}\oint_{\mathcal{C}} \tau ds, \tag{19}$$

and $Tw = \tau L/2\pi = \mathcal{H}/\Gamma^2$. (Note that τ need not be independent of z; the case where $\tau = \tau(z,t)$ will be considered in a later section, z-Dependent Twist Distributions).

Now we can use the vorticity evolution equation to understand how $\tau(r,t)$ evolves, checking whether or not it tends towards a constant in r over time. Approaching the two components of the vector diffusion equation separately, we first use the z component to find a partial differential equation for $\Omega(r,t)$:

$$\dot{\Omega}(r,t) = \frac{\nu}{r}\left(\Omega'(r,t) + r\Omega''(r,t)\right) \tag{20}$$

where dots and primes correspond to partial time and space derivatives respectively. Naturally, Gaussian distributions are solutions to this evolution equation, since it is derived from a diffusion equation, indicating that even an initial vorticity profile that is not Gaussian will tend towards a Gaussian profile over time. We will thus take $\Omega(r,t)$ to be given by

$$\Omega(r,t) = \frac{\Gamma}{\pi a^2(t)} e^{-r^2/a^2(t)}, \quad a(t) = \sqrt{4\nu t + a_0^2} \tag{21}$$

where a_0 is the initial core size of the vortex tube at its creation at time $t = 0$ and will be set to $a_0 = 2$ along with $\nu = 1$ for the following calculations.

The azimuthal component of the diffusion equation provides an evolution equation for $\tau(r,t)$ in terms of its derivatives, as well as Ω and its derivatives:

$$\frac{\dot{\tau}}{\tau} = \frac{\nu}{r}\left(3\frac{\tau'}{\tau} + 2\frac{\Omega'}{\Omega} + 2r\frac{\Omega'}{\Omega}\frac{\tau'}{\tau} + r\frac{\tau''}{\tau}\right), \tag{22}$$

which can be simplified by plugging in $\Omega'/\Omega = -2r/a^2$, assuming a Gaussian profile. Doing so yields

$$\frac{\dot{\tau}}{\tau} = \frac{\nu}{r}\left(3\frac{\tau'}{\tau} - 4\frac{r}{a^2} - 4\frac{r^2}{a^2}\frac{\tau'}{\tau} + r\frac{\tau''}{\tau}\right). \tag{23}$$

This partial differential equation for τ can then be integrated numerically to find solutions for each $\tau(r,t)$, assuming an initially Gaussian $\Omega(r,t)$ profile and some arbitrary initial linear twist density profile $\tau_0(r)$.

Two different initial linear twist density profiles are evolved, the first corresponding to a Gaussian addition on top of the uniform twist:

$$\tau_0^{(1)}(r) = 1.0 + e^{-r^2/a_0^2}, \tag{24}$$

while the second has a more complex twist profile:

$$\tau_0^{(2)}(r) = 1.0 + 2\left(\cos\left(\frac{2\pi r}{a_0}\right) - \frac{1}{2}\right) e^{-r^2/a_0^2}. \tag{25}$$

In each case, the linear twist density profiles decay to “uniform twist” states, regardless of the details of the initial state (Figs. S6, A and D). Over the course of this decay, the percent error in the helicity as measured by the center-line flow relative to the volumetric helicity decays. The shape of this decay is well fit by

$$f(t; a, b, c) = \frac{a}{bt + c} \tag{26}$$

indicating that each of these non-uniform twist states will tend towards a “uniform twist” state like $1/t$, such that even vortices that do not initially satisfy the “uniform twist” condition will tend to over time.

Examination of Small Core Assumption

To understand the extent to which the failure to achieve sufficient separation of scales between the core size and curvature of the vortex tube results in an error in our helicity measure, we simulate a writhing vortex tube and track the helicity measures, core size, and curvature over time. The simulations are performed with the specifications detailed in Materials and Methods.

To generate an initial state for a writhing vortex tube, first a straight vortex column spanning the periodic length L of the simulation domain was generated from the analytic expression

$$\vec{\omega} = \Omega(r)\left(\hat{z} + \tau r \hat{\phi}\right), \tag{27}$$

where $\Omega(r)$ is the cross-sectional profile of the vortex core and τ is the linear twist density, related to the overall twist, Tw, via:

$$Tw = \frac{1}{2\pi}\int_0^L \tau(z)\, dz. \tag{28}$$

The form of $\Omega(r)$ was chosen to be Gaussian due to the presence of viscous effects, and is given by

$$\Omega(r) = \frac{\Gamma}{\pi a^2} e^{-r^2/a^2}, \tag{29}$$

where the circulation is $\Gamma = 2.5$, the core size is $a = L/20$, and τ is taken to be a constant such that $Tw = Wr$, where $Wr = 0.013$ is the writhe of the desired helical initial condition. The Reynolds Number for the simulation is $Re = \Gamma/\nu = 2500$.

This straight tube was then convected by an incompressible flow until its center-line is described by

$$\vec{X}(x, y, z) = (R\cos(kz), R\sin(kz), z), \tag{30}$$

where $Rk = 0.163$, $k = 2\pi$, and $z \in [0, 1]$, resulting in our initial state. Because this process does not change the topology of the field-lines, the resulting writhing state has the same helicity as the straight, twisted vortex column. The state is then evolved according to the specifications outlined in Materials and Methods (Movies S4 and S5).

For each time step of the simulation, the vortex center-line was extracted by first identifying a single vortex surface by tracing a vortex field-line as it traverses the periodic domain many times, and then iterating this process inside the reconstructed surface until it returns a line. From this center-line, we measured $\Gamma \oint \vec{u} \cdot d\vec{\ell}$ for the helix and compared it to the helicity of the volume (Fig. S7E). The two curves show strong agreement, beginning in a sub-percent error regime. As the core size grows with diffusion, the separation of scales between the core size and curvature worsens and this small error increases to a few percent. To quantify the relationship between this error and the scale separation, we measured each of these scales at various time steps in the vortex evolution. The core size a is measured by fitting the vorticity profile on a slice normal to the center-line to a 2D Gaussian:

$$f(r; \Gamma, a) = \frac{\Gamma}{\pi a^2} e^{-r^2/a^2}. \tag{31}$$

The curvature κ was computed by taking the magnitude of the derivative of the tangent vector along the center-line. We then compare how the scale trends with the error in our helicity measure (Figs. S7, C and D).

To estimate the potential error due to the thickness of our experimental vortices, we can estimate the separation of scales in the experiment. The curvature at each point on the path can be computed numerically at each time step of each experiment, and the median of these values is taken as the effective curvature for the path at that point in time. To find the core size throughout the evolution, we assume an initial core size and then numerically integrate the following differential equation for the core size:

$$\dot{a} = \frac{2\nu}{a} - \frac{\dot{L}}{2L}a, \tag{32}$$

where the first term corresponds to viscous diffusion of the core, while the second corresponds to thinning or fattening of the core due to volume conservation of the vortex tube as the vortex is stretched or compressed.

Possible values of $a\kappa$ over the duration of three typical experiments are computed, one for each geometry considered in the main text (Figs. 8, A to C). For an initial core size of $a_0 = 1mm$, the value of $a\kappa$ peaks near 0.2, placing the error on the order of $\sim 10\%$. We note that this error is within the reproducibility of our experimental trials.

z-Dependent Twist Distributions

Our previous discussion of twist has been limited to linear twist densities that are independent of z, i.e. $\tau = \tau(r,t)$. To investigate the possible influence of having $\tau = \tau(z,t)$ on our total helicity measure, we simulated a straight, twisted vortex core with an initial state corresponding to

$$\vec{\omega} = \Omega(r)\left(\hat{z} + \tau(z)r\hat{\phi}\right), \tag{33}$$

where the profile is still given by

$$\Omega(r) = \frac{\Gamma}{\pi a^2}e^{-r^2/a^2}, \tag{34}$$

with $a = L/10$, but now the linear twist density is given by

$$\tau(z) = 1 + \frac{1}{2}\sin\left(2\pi z/L\right). \tag{35}$$

The results of the simulation are summarized in Figure S9 (Movies S6 and S7). The near perfect agreement between the volumetric and center-line measures of the total helicity indicate that variations in the linear twist density along the length of the vortex tube alone do not jeopardize the accuracy of the measurement, and further do not cause the vortex column to move away from a state of "uniform twist", as evidenced by the consistent flatness of the ratio of poloidal to toroidal flux as you move away from the center-line (Figs. S9, D to F).

Twist Dissipation in General Vortex Tubes

In the presence of viscosity, the rate of change of helicity is no longer identically zero, and is instead given by

$$\dot{\mathcal{H}} = -2\nu \int_V \vec{\omega} \cdot \vec{\nabla} \times \vec{\omega} \, dV, \tag{36}$$

where ν is the viscosity and the integral is performed over the entire volume (*1*). The integrand depends on both the geometry of the vortex field-lines and the vorticity profile across the vortex surfaces, a point which can be made explicit by substituting $\vec{\omega} = |\vec{\omega}|\hat{\omega}$ into the integral, which gives

$$\dot{\mathcal{H}} = -2\nu \int_V \hat{\omega} \cdot \vec{\nabla} \times \hat{\omega} \, |\vec{\omega}|^2 dV. \tag{37}$$

This result indicates that for the same field structure, determined entirely by the tangent field $\hat{\omega}$, different rates of change of helicity can be achieved by changing the spatial profile of the vorticity magnitude; on the other hand, keeping the vorticity intensity fixed, the underlying field geometry can be altered to change $\dot{\mathcal{H}}$, and thus, the rate of twist dissipation. Here we consider a variety of vortex tubes and show that predicting the twist dissipation rate requires detailed information about both $|\vec{\omega}|^2$ and $\hat{\omega}$—more than just the average core size or total twist—demonstrating that the local details of the vortex core influence how fast helicity changes via twist dissipation.

We begin by computing the dissipation for a uniformly twisted, straight vortex tube whose linear twist density, τ, has no z dependence. Under these constraints, Equation S23 for the evolution of the twist density simplifies and can be solved for $\tau(t)$, giving

$$\tau(t) = \frac{\tau_0}{4\nu t/a_0^2 + 1}, \tag{38}$$

which allows us to write down an analytic expression for the helicity in this simple case:

$$\frac{\mathcal{H}(t)}{\Gamma^2} = \frac{\mathcal{H}_0}{\Gamma^2}\frac{1}{4\nu t/a_0^2 + 1}. \tag{39}$$

Note that because the only helicity is twist helicity, this expression gives the time evolution for the twist. The first case that we can attempt to extend this understanding to is the case of a straight-line vortex with a linear twist density that varies along its length, i.e. $\tau = \tau(z,t)$. Using the data from the simulation of a twisted tube performed in the previous section, we fit the helicity of the tube with a function of the form

$$f(t; a, b) = \frac{a}{bt + 1}. \tag{40}$$

We see strong agreement between the data and the fit (dash-dotted purple line, Fig. S9C), despite the fact that the twist is evolving along the z direction in the simulation, while our calculation assumed a linear twist density constant along the vortex length. The fit parameters are well matched to the physical parameters: in the simulation

$$\frac{\mathcal{H}_0}{\Gamma^2} = 9.79 \times 10^{-2}, \quad \frac{4\nu}{a_0^2} = 0.4, \tag{41}$$

which should be matched to the fit parameters

$$a = 9.81 \times 10^{-2}, \quad b = 0.405 \tag{42}$$

respectively. We thus see that the twist dissipation rate in a straight line vortex with variable linear twist density can be characterized by ν/a_0^2.

To expand our discussion of the dependencies of the twist dissipation rate to include curved center-line geometries and variable core profiles, we numerically compute $\dot{\mathcal{H}}$ for a variety of helical and undulating vortices. We note that $\dot{\mathcal{H}}$ instantaneously captures exactly the twist dissipation for single loops, since any changes in writhe due to geometric deformations will be instantaneously offset by compensating twist production, producing no net contribution to $\dot{\mathcal{H}}$; thus, any non-zero contribution to $\dot{\mathcal{H}}$ at $t = 0$ is due exclusively to the dissipation of twist by viscous effects.

Two groups of vorticity fields were considered: the first contains curved and helical vortex tubes, while the second group contains straight-line vortices with an imposed core width modulation. For curved vortex tubes, we generate analytic expressions for the flow and vorticity fields using complex scalar fields as in (*59*), which yields divergence-free vector fields whose field-lines lie on surfaces organized around a chosen center-line. This construction enables us to tune the writhe of the center-line, and to control the twisting of the field-lines around the center-line independently of each other.

This analytical construction (*59*) is based on a complex scalar field $\psi = u^m/Q(u, u^*, v, v^*)$ where (u, v) are coordinates on S^3, the complex polynomial $Q(u, u^*, v, v^*)$ encodes the chosen center-line in its nodal set, and m controls the winding of the field-lines around the center-line. The vorticity field is given in terms of the complex scalar field ψ as follows:

$$\begin{aligned}\vec{\omega} &= \nabla\left(\frac{\psi\,\psi^*}{1+\psi\,\psi^*}\right) \times \frac{1}{4\pi i}\nabla \log\left(\frac{\psi}{\psi^*}\right) \\ &= \frac{1}{2\pi}\nabla\chi \times \nabla\eta\end{aligned}$$

where $\chi = (\psi\,\psi^*)\,/\,(1 + \psi\,\psi^*)$, $\chi \in [0, 1]$ labels the vortex surfaces, and $\eta = \frac{1}{2i}\log(\psi/\psi^*)$, $\eta \in [0, 2\pi)$ is akin to an angle about the center-line.

To mimic a Gaussian core profile in our analytical construction, we map χ to a radial distance r using a 1D analogue of the stereographic projection which takes values between 0 and ∞ as follows: $\chi = \frac{1}{1+r^2}$. A Gaussian core profile can then be expressed in terms of χ using the above mapping as $f(\chi) = \frac{1}{2\chi^2}\exp(-\frac{1-\chi}{a^2\,\chi})$, where a is the clipping length scale. We obtain vorticity distributions resembling a Gaussian core profile by multiplying the vorticity field above by $f(\chi)$ to give the new vorticity field, restricted to a vortex tube:

$$\vec{\omega} = \frac{f(\chi)}{2\pi}\nabla\chi \times \nabla\eta$$

$$= \frac{1}{4\pi\,\chi^2} \exp\left(-\frac{1-\chi}{a^2\,\chi}\right) \nabla\chi \times \nabla\eta. \tag{43}$$

The resultant tubes are roughly Gaussian, with a modulation along the length of the vortex that vanishes in the limit of small amplitude helices. Following the ideas outlined in (*59*), the velocity field associated with the above vorticity field is given by:

$$\vec{u} = \frac{a^2}{4\pi}\Bigg(\exp\left(-\frac{1-\chi}{a^2\,\chi}\right) \nabla\eta + \frac{1}{2i}\nabla \log\left(\frac{Q(u,u^*,v,v^*)}{Q^*(u,u^*,v,v^*)}\right)\Bigg). \tag{44}$$

As a result of this construction, all of the vortex tubes produced with this method satisfy the "uniform twist" condition and thus have helicity given by

$$\mathcal{H} = \Gamma \oint_C \vec{u} \cdot d\vec{\ell}. \tag{45}$$

To expand our survey beyond helical shapes, we also consider straight-line vortices with prescribed core modulations. To generate the vorticity fields of these straight-line vortex tubes, we used the following expression to generate a variety of initial states:

$$\vec{\omega} = \frac{\Gamma}{\pi a(z)^2} e^{-r^2/a^2(z)} \left(\hat{z} + r\tau\hat{\phi} + r\frac{a'(z)}{a(z)}\hat{r}\right), \tag{46}$$

where the profile is $a(z) = a_0 + A\sin(2\pi z/L)$, the core size is $a_0/L = 0.1$, the linear twist density is $\tau = 2\pi/10$, and the amplitude of the undulation A includes $0.25a_0$ along with values ranging from $0.3a_0$ to $0.7a_0$ in steps of $0.1a_0$. All initial states constructed with this method satisfy the "uniform twist" condition. The states with $A = 0.25a_0$ and $A = 0.5a_0$ were simulated according to the specifications outlined in Materials and Methods, over time producing additional collections of straight-line vorticity fields, which we also sample.

For each field considered, the dissipation rate, $\dot{\mathcal{H}}$, is computed via Equation S36, while the twist is defined as $Tw = \mathcal{H}/\Gamma^2 - Wr$ (since there is no tube linking) and the mean core size, $\bar{a}$, is computed by averaging the profile width along the tube. Each dissipation rate is then normalized by $-4\nu/\bar{a}^2 \times \Gamma^2 Tw$, the twist dissipation rate of a straight twisted Gaussian vortex of uniform core size $\bar{a}$ (Fig. S10 A and E). The spread in the normalized twist dissipation rates observed in both the curved and straight vortex tubes indicates that the detailed interplay between $|\vec{\omega}|^2$ and $\hat{\omega}$, not just the average core size and total twist, play a role in determining the rate at which twist is dissipated.

Estimating Dissipation using Dimensional Analysis

Estimating the rate of change of helicity using dimensional analysis is made difficult by the fact that the appropriate length scales are not straightforwardly associated with gradients of the flow, but are in fact better captured by the geometry of the vorticity field-lines.

The difficulty in performing a straightforward gradient-based estimation can be underscored through the simple example of a straight twisted vortex tube, for which we can attempt to estimate the dissipation rate and then compare our result to the analytic answer. Consider a vortex of length L whose vorticity is given by

$$\vec{\omega} = e^{-r^2/a^2}\left(\hat{z} + \frac{2\pi}{L} r\hat{\phi}\right) \tag{47}$$

such that the twist is given by $Tw = 2\pi/L \times L/2\pi = 1$ and its helicity is $\mathcal{H} = Tw\Gamma^2 = \Gamma^2$. Now we can attempt to recover the relative dissipation rate $\dot{\mathcal{H}}/\mathcal{H}$ up to a pre-factor using dimensional analysis. Beginning with the dissipation integrand, we make the substitution

$$\vec{\omega} \cdot \vec{\nabla} \times \vec{\omega} \sim \frac{\omega^2}{a} \tag{48}$$

where the core size a has been used to estimate the length scale of the gradient. Integration over the volume will produce a factor of La^2, allowing us to write

$$\dot{\mathcal{H}} = -2\nu \int \vec{\omega} \cdot \vec{\nabla} \times \vec{\omega}\, dV \sim \nu \frac{\omega^2}{a} a^2 L. \tag{49}$$

Noting that $\Gamma \sim \omega a^2$ and dividing by $\mathcal{H} = \Gamma^2$, we arrive at our estimation of the dissipation rate using the scales associated with core gradients:

$$\frac{\dot{\mathcal{H}}}{\mathcal{H}} \sim \frac{\nu}{a^2} \frac{L}{a}. \tag{50}$$

Computing $\dot{\mathcal{H}}/\mathcal{H}$ explicitly for this configuration, however, gives

$$\frac{\dot{\mathcal{H}}}{\mathcal{H}} = \frac{4\nu}{a^2}, \tag{51}$$

which upon comparison to Equation S50 shows that our estimate based on gradients in the flow gives the incorrect dependence on the core size and the length of the vortex, indicating that this line of reasoning doesn't recover the appropriate dissipation behavior.

Had we instead estimated the dissipation integrand to be

$$\vec{\omega} \cdot \vec{\nabla} \times \vec{\omega} \sim \frac{\omega^2}{L} \tag{52}$$

we could carry out the remaining steps as before and arrive at the correct dependence for the dissipation rate, i.e. $\dot{\mathcal{H}}/\mathcal{H} \sim \nu/a^2$. This indicates that the correct length scale for the integrand is not that associated with a core gradient; it is instead the length scale associated with a geometric feature of the vortex, namely the wavelength of the twisting of the vortex field-lines λ (here, given by L) along the length of the vortex (a direction in which there are no gradients). Thus, dissipation cannot be captured with simple dimensional analysis, since the field-geometry not only influences the pre-factor for the dissipation but also the quantities on which it depends.

Implicit in our ability to identify a wavelength or pitch associated with the twisting of field-lines is the existence of some frame defined along the vortex that we can measure this winding relative to. In the straight line case, this framing is so natural that we did not even need to explicitly define it and assumed it to be given by the tangent vector and two normal vectors that do not rotate about the tangent as you move along the center-line, say $(\hat{x}, \hat{y})$ in our example above. If the vortex instead writhed in space, the choice of framing becomes less clear. Here we show that field-lines that follow the parallel transport framing contain no local twist, indicating that the parallel transport framing is the correct reference frame for isolating the twist and its length scale. Furthermore, we show that $\dot{\mathcal{H}}$ for such a twist-free vortex is zero.

We can start by constructing a bundle of field-lines organized around a center-line that follow the parallel transport framing. Consider a center-line path that writhes in space defined by $\vec{x}(s)$. At a point defined by s_0 on this path, we can construct a plane normal to the tangent, $\hat{t}(s_0)$, at that point. We can then construct a set of basis vectors, $(\hat{a}, \hat{b})$, in this plane by first picking an arbitrary vector, say $\hat{x}$, and taking

$$\hat{a} = \hat{t}(s_0) \times \hat{x}, \tag{53}$$

$$\hat{b} = \hat{t}(s_0) \times \hat{a}, \tag{54}$$

such that any point in that plane is connected to $\vec{x}(s_0)$ by $\vec{c} = \alpha\hat{a} + \beta\hat{b}$, where $\alpha^2 + \beta^2 \leq R$, the radius of the cross-section. (Additionally, we require that $R\kappa < 1$ at each point on the path to prevent cross-sections from intersecting.) We can then think of the choice of (α, β) as selecting different field-lines in the vortex bundle, located relative to the center-line by the vector $\vec{c}$.

Points that lie on the same field-line but on different cross-sections of the vortex bundle can be associated with each other by transporting the vector $\vec{c}$ from the cross-section at s_0 to that passing through $s_0 + \epsilon$. To do so, we transport the vector to $\vec{x}(s_0 + \epsilon)$, subtract off the component along the new tangent, and then rescale the vector to have the same length as before, i.e.

$$\vec{c}(s_0 + \epsilon) \quad = \frac{\vec{c}(s_0) - \left(\vec{c}(s_0) \cdot \hat{t}(s_0 + \epsilon)\right)\hat{t}(s_0 + \epsilon)}{|\vec{c}(s_0) - \left(\vec{c}(s_0) \cdot \hat{t}(s_0 + \epsilon)\right)\hat{t}(s_0 + \epsilon)|} |\vec{c}(s_0)|.$$

Iterating this process for a single initial choice traces out a field-line in our bundle, identified by the normal vector $\vec{c}(s)$ at each slice. On a cross-section of the bundle perpendicular to the centerline, all the field-lines in the bundle are aligned with the center-line of the bundle. We compute the tangent to a field-line intersecting the cross-section at s_0 at the point $\vec{x}(s_0) + \vec{c}(s_0)$:

$$\begin{aligned} \hat{t}(\vec{c}(s_0)) \quad &\propto \quad \hat{t}(s_0) + \lim_{\epsilon \to 0} \frac{\vec{c}(s_0 + \epsilon) - \vec{c}(s_0)}{\epsilon} \\ &\propto \quad \hat{t}(s_0) - \left(\vec{c}(s_0) \cdot \partial_s \hat{t}(s_0)\right) \hat{t}(s_0) \\ &\propto \quad \hat{t}(s_0). \end{aligned} \tag{55}$$

The resulting bundle follows the parallel transport framing, since the field-lines do not locally rotate about the tangent vector, i.e. $\partial_s \hat{c} \cdot \left(\hat{c} \times \hat{t} \right) = 0$ at each point along the path. To prove this, we can compute the triple product in the limit $\epsilon \to 0$:

$$\partial_s \hat{c} \cdot \left(\hat{c} \times \hat{t} \right) = \lim_{\epsilon \to 0} \left(\frac{\hat{c}(s+\epsilon) - \hat{c}(s)}{\epsilon} \right) \cdot \hat{c}(s) \times \hat{t}(s).$$

Plugging in our expression for $\hat{c}(s+\epsilon)$ and expanding $\hat{t}(s+\epsilon) = \hat{t}(s) + \epsilon \partial_s \hat{t}$ we find

$$= -\left(\vec{c}(s) \cdot \partial_s \hat{t} \right) \hat{t}(s) \cdot \left(\hat{c}(s) \times \hat{t}(s) \right) = 0,$$

indicating that this construction is indeed parallel transported and locally twist-free.

Furthermore, since there always exists a surface perpendicular to such a vortex bundle, $\vec{\omega} \cdot \nabla \times \vec{\omega} = 0$ by Frobenius' theorem (*60*). Hence such a vortex bundle configuration has a vanishing $\dot{\mathcal{H}}$.

Estimation of Experimental Error Incurred in Center-line Identification

For a vortex tube that satisfies the requisite core structure assumptions outlined in the supplementary text section Calculation of Total Helicity, there remain two main sources of experimental error in calculating the total helicity: the error in the recovery of the correct center-line for each vortex tube; and the error in sampling the velocity on a given center-line path. Here we estimate the contribution from the first of these two sources, leaving the second for the following section.

To estimate the degree to which the center-line extracted from the experimental data could be offset from the correct center-line, we first note that for a vortex with a Gaussian vorticity profile a blob of dye offset from the center-line will experience shear, and that this shear will smear the blob into an annular structure in the cross-sectional intensity pattern of the vortex (Figs. S12, A to C). It is clear that for experimental trials no such annulus can be resolved in the vortex cross-sections (Fig. S12D); instead a dot with a roughly Gaussian profile is observed (Fig. S12E). This could be due to one of two scenarios: either, the annulus could be formed, but is too small to be resolved; or the blob is not far enough away from the center-line to experience enough shear in the time prior to observation to form an annulus. We can calculate the bound on the blob offset from each of these cases and used the larger one as an estimate of the center-line position error.

First we consider the possibility that the blob experiences sufficient shear to form an annulus, but forms a structure that is too small to distinguish from a Gaussian bump. In this case, we can assume that the Gaussian intensity profile $I(r)$ resolved is the superposition of two overlapping, opposite sections of the annulus, each of which are Gaussian, i.e.

$$I(r) = I_0 e^{\frac{-r^2}{2\sigma^2}} \sim a e^{\frac{-(r-b)^2}{2c^2}} + a e^{\frac{-(r+b)^2}{2c^2}}. \tag{56}$$

To infer the separation b of the underlying Gaussians (and thus the blob offset from the center-line), we can solve for the greatest value of b for which the superposition of Gaussians has an inflection point at $r = 0$ (indicating that any further away, there would be positive curvature and the maximum of the intensity profile would no longer be at the center). Doing so sets an upper bound of $b = c$ for the underlying Gaussians, which can then be related to σ of the measured intensity distribution by equating it to the half-width half-max of the superposition, which gives the following expression for b in terms of σ:

$$b = \frac{\sigma}{1 + \sqrt{1 + 2\ln(2)}}. \tag{57}$$

This gives an upper bound estimate on the possible blob displacement from the center-line of $b = \delta \sim 0.26mm$ or $\delta/a \sim 13\%$ for $a = 2mm$.

Second, we consider the possibility that, rather than forming an annulus too small to be resolved, instead the blob was seeded at a location where the shear is not sufficient for annulus formation. In this case, the upper bound for the offset is given by the furthest the blob could be from the center-line and just form an annulus. To put a numerical bound on this distance, we first assume that the vortex has a Gaussian core structure, such that the azimuthal angular velocity $\omega(r) = u_\phi/r$ is given by

$$\omega(r) = \frac{\Gamma}{2\pi r^2}(1 - e^{-r^2/a^2}) \tag{58}$$

where Γ and a are the circulation and core size, respectively. Since this angular velocity is monotonically decreasing from the center of the vortex, for a blob of width $2r_b$ centered a distance δ away from the center-line, the maximal shear is experienced between the nearest and furtherest parts of a blob. The difference between angular speeds for these two points is given by

$$\Delta\omega(\delta) = \omega(\delta - r_b) - \omega(\delta + r_b). \tag{59}$$

In terms of the offset δ, the time elapsed prior to observation Δt, and the angular velocity difference $\Delta\omega$, the condition for annulus formation can be written:

$$\Delta\omega(\delta)\Delta t \geq 2\pi. \tag{60}$$

For our experimental parameters, we can invert this equation to find the limiting value for δ, the furthest the blob could be offset without forming a complete annulus. The most conservative error is achieved by using the lowest circulation examined $\Gamma \sim 12,000mm^2/s$, the typical time between generation and the first acquisition $\Delta t = 0.11s$, and a core size of $a = 2mm$. Doing so gives

$$\delta \leq 0.4mm \Rightarrow \delta/a \sim 20\%. \tag{61}$$

It is true that distances multiple core sizes away from the center-line also satisfy the no-annulus-formation condition (for the parameters above, this is $\delta/a \sim 2.25$); however, the dynamics of the dyed path would then be inconsistent with Biot-Savart evolution, which our experiments are not.

We see then that the possibility of placing the dye in a region with weak shear represents the larger offset, and thus error, for the two possible situations, providing an upper bound on the displacement of the center-line to be $\sim 20\%$ of the core size.

Given this upper-bound for the displacement, we can use numerical data for the vorticity and flow fields of a vortex column with z-dependent twist (detailed in section z-Depends Twist Distributions) to translate this offset into an expected error in the helicity measurement. Incorrect center-line paths through the vortex core are generated by superposing five helical paths around the center-line, each of which has a random phase between 0 and 2π and a random wavenumber between 0 and 10. The mean offset of the resultant random path from the correct center-line is then calculated by averaging the distances between the center-line and the random path in each normal cross-section of the vortex column. The difference between the actual helicity and the helicity measured from the random path is then computed and plotted against the mean offset from the center-line (Fig. S12F). The data is then binned, providing an average percent error for a given mean offset relative to the core size.

From this data we see that for offsets of $\delta/a \sim 20\%$, we expect errors in identifying the correct center-line path to contribute on average an error on the order of $\sim 1\%$ of the total helicity.

Estimation of Experimental Error Incurred in Velocity Sampling

To track the blobs inside the vortex core, the intensity values inside the tube were summed in the transverse directions to produce a 1D intensity profile along the center-line. While this process is important for producing robust peak tracking, it will effectively average the fluid velocity over a small region around the center-line, instead of reporting exactly the value at the center-line. Here we estimate the potential error from this procedure by examining the contributions from three distinct types of flows: (a) non-local, self-induced flows, (b) non-local, non-self-induced flows, (c) local, self-induced flows.

(a) Non-local, self-induced flows: A small segment of the vortex tube will feel the flow generated by both the segments in its immediate vicinity and by segments far from it in terms of path length distance. The nearby segments will in general produce a flow in the binormal direction, normal to the tangent of the center-line, such that this flow will not contribute to the integrand of the experimental helicity measure.

The distant vortex segments, however, can produce flows tangent to the vortex tube.

Assuming the alignment between the flow and the center-line is maximal and that the distant segments are on average the root-mean-squared radius $\bar{r}$ away, the tangential flow from these regions is given by $u_t = \Gamma/2\pi\bar{r}$. The velocity that our measurement reports is then the average of this velocity over the extruded tube of edge length $2d$, i.e. between $\bar{r} - d$ and $\bar{r} + d$. In the regime where $d/\bar{r} \ll 1$, we can write the averaged velocity $\bar{u}$ as

$$\bar{u} = \frac{1}{2d}\int_{\bar{r}-d}^{\bar{r}+d} \frac{\Gamma}{2\pi r} dr \sim \frac{\Gamma}{2\pi\bar{r}} \left(1 + \frac{1}{3}\left(\frac{d}{\bar{r}}\right)^3 + \mathcal{O}\left(\frac{d}{\bar{r}}\right)^5\right) \tag{62}$$

We see that for flows of this form, this average is exact to the third order in $d/\bar{r}$, which for the isolated helix, is roughly $(1/60)^3 \sim 1 \times 10^{-6}$.

(b) Non-local, non-self-induced flows: The vortex will also experience small flows from residual effects inside the tank associated with submerging the hydrofoil at the start of the experiment as well as residual flows from previous experiments. By Stoke's theorem, these flows will only have a net contribution to the contour integral for the helicity if they are generated by vortex field-lines that are linked with the experimental vortex. Using buoyant micro-bubbles as tracers that dynamically aggregate on vortices, we can verify the absence of any vortices linked with the experimental vortices, such that we expect no net contribution to the integral from non-local, non-self-induced flows.

(c) Local, self-induced flows: Twisting of the vortex field lines will generate a local, axial flow along the vortex tube center-line. For a tube with constant linear twist density and a Gaussian vorticity profile, this axial flow has a Gaussian profile across the core, given by

$$u_t = \frac{\tau\Gamma}{2\pi} e^{-r^2/a^2}. \tag{63}$$

where τ is the linear twist density. Taking the average of this flow over a window of width $2d$ centered on the center-line, we find

$$\bar{u} = \frac{\tau\Gamma}{2\pi} \left(1 - \frac{1}{3}\left(\frac{d}{a}\right)^3 + \mathcal{O}\left(\frac{d}{a}\right)^5\right) \tag{64}$$

which for a core size of $a \sim 2mm$ and a window of $2d \sim 1mm$ results in a $\sim 1\%$ reduction in the measured velocity as compared to the exact center-line velocity.

Helicity Values of Planar Loops

In all cases, the starting writhe and total helicity for experimentally generated planar rings is zero and remains zero over the course of their evolution and interaction with other, even helical, vortices (Figs. S13, A and C). The constant zero values of the total and component helicities indicates that while the helicity of the partner helix may be evolving in a complicated way, there is minimal or no transfer of helicity between the distinct loops throughout these processes at these scales.

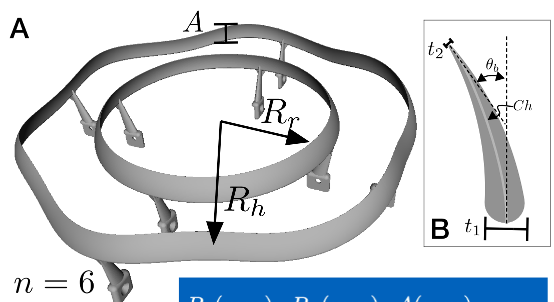

	$R_r(mm)$	$R_h(mm)$	$A(mm)$	n
Isolated Helix	N/A	72	4.3	6
Compression	72	120	4.9	6
Stretching	120	72	5.4	9

Figure 1: Hydrofoil parameters. **(A)** An example hydrofoil mesh with the relevant experimental parameters labeled. Values for each parameter used in the three types of experiments are listed in the accompanying table. **(B)** The cross-section used for all hydrofoils. In all cases, $Ch = 15mm$, $\theta_b = 35°$, $t_1 = 3.125mm$, and $t_2 = 0.188mm$.

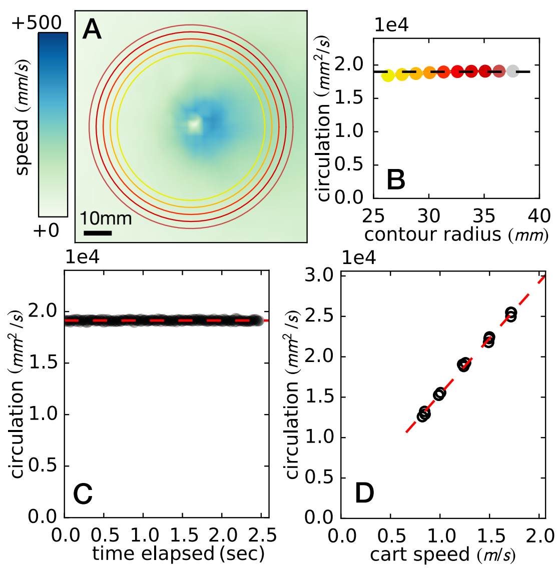

Figure 2: Vortex circulation calibration. **(A)** Magnitude of flow velocity in a cross-section centered on an isolated, helical vortex. Colored rings indicate various contours along which the flow field is integrated (every other shown). **(B)** Values for the circulation integrals for contours. Colors match subset of contours shown in (A). The dotted line indicates the average of measured values and is taken to be the circulation, Γ, of the vortex at that moment in time. **(C)** Circulation values for a vortex recorded over its evolution. **(D)** Time averaged circulation values plotted against the final hydrofoil speed for 15 trials. The dotted line is a linear fit to the data.

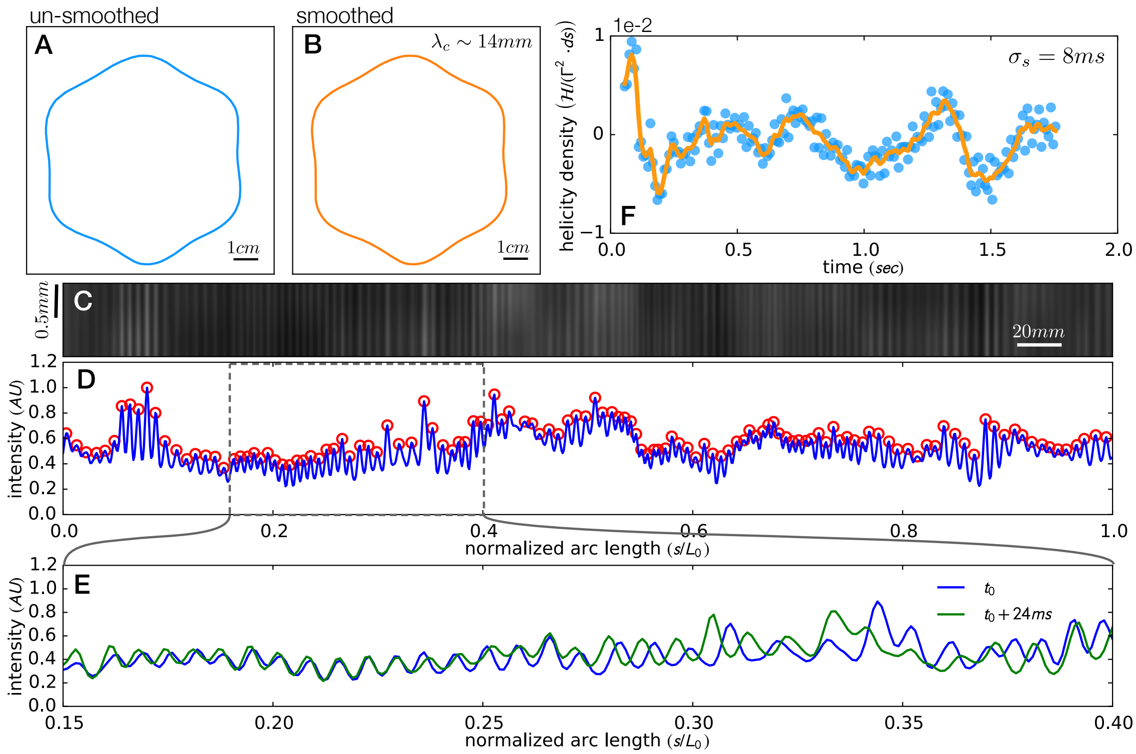

Figure 3: Blob identification and tracking procedure. **(A and B)** After being traced from each volume, the raw path (A) is smoothed using a sinc filter with a cutoff frequency of $\lambda_c \sim 14mm$, producing the smoothed path (B). **(C)** The volume around the smoothed path, flattened by summing over one of the two transverse directions. **(D)** The intensity profile along the path after summing over both the transverse dimensions. The open circles indicate the identification of a blob. **(E)** A comparison between intensity profiles over a sub-section over the vortex path, separated by 24ms. Trackpy is used to track the peaks over time. **(F)** The contribution to the total helicity from a single blob over time. The blue dots represent the raw dimensionless helicity density values $\vec{u} \cdot \hat{t}/\Gamma$, while the gold line is the result of convolving the data with a Gaussian of standard deviation $\sigma_s = 8ms$.

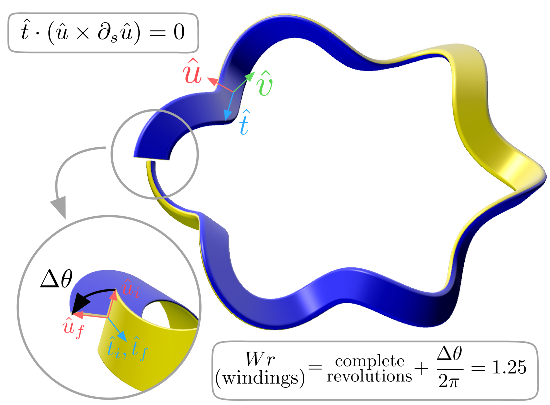

Figure 4: A ribbon writhing in space. The basis triad for the ribbon $(\hat{t}, \hat{u}, \hat{v})$ is illustrated with blue, red, and green vectors. The ribbon is everywhere untwisted. The angle by which the ribbon is over-wound when it returns to the start is $\Delta\theta$.

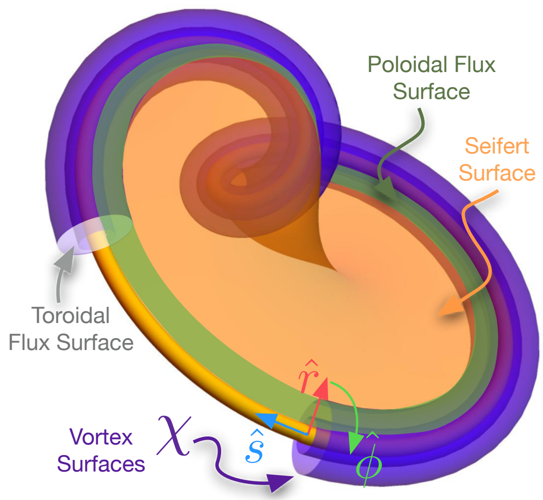

Figure 5: Surfaces associated with thin-core vortex tubes. The solid, gold tube shows the center-line path, around which purple vortex surfaces are nested (shown with a cutaway for clarity). An example surface used for computing the toroidal flux is shown in white spanning the cross-section of one such vortex surface. A Seifert surface for the center-line is shown in orange. The portion of the Seifert surface that falls within the outermost vortex surface shown is highlighted in green and is the poloidal flux surface for that vortex surface.

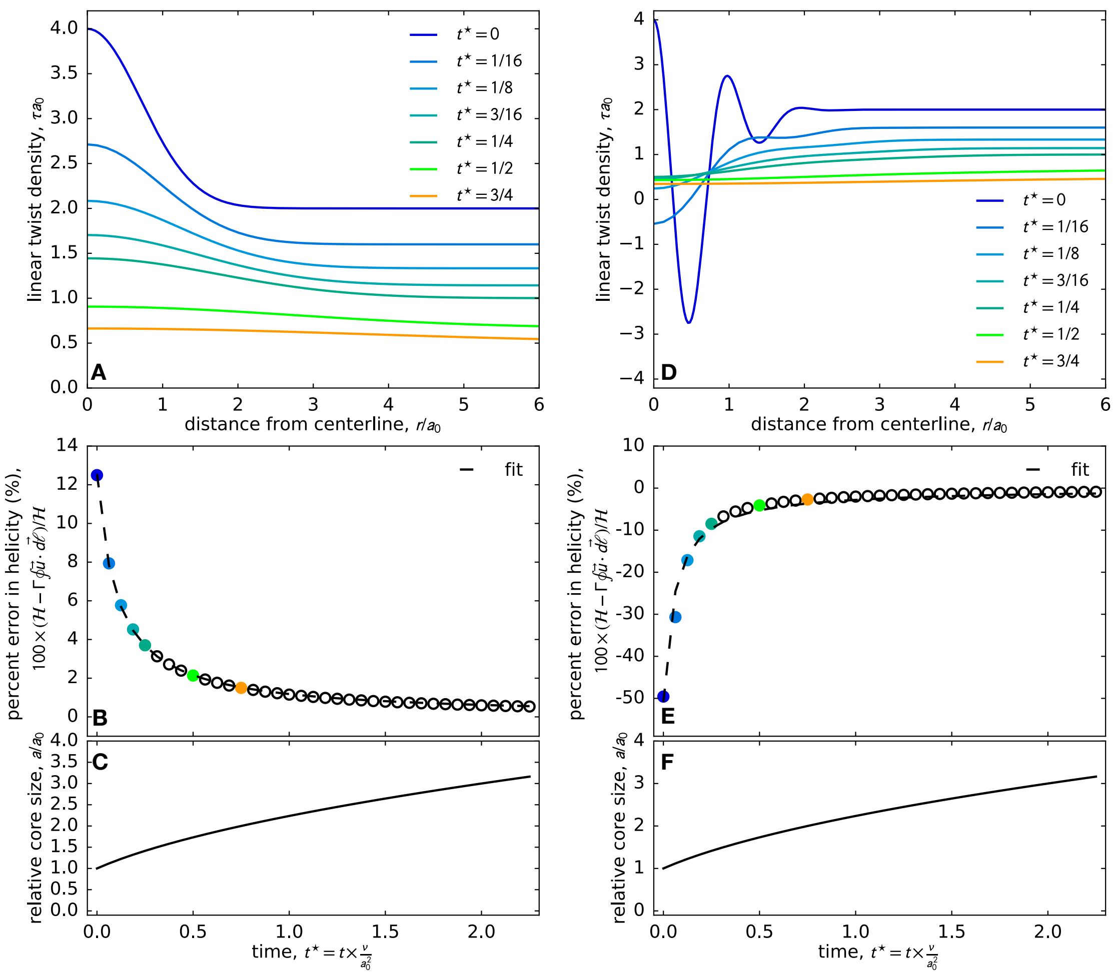

Figure 6: Linear twist density $\tau(r,t)$ evolution in straight non-uniformly twisted vortex cores. **(A and D)** Snapshots of τ profiles for a variety of times for $\tau_0^1(r) = 1.0 + e^{-r^2/a_0^2}$ and $\tau_0^2(r) = 1.0 + e^{-r^2/a_0^2} \times 2(\cos(2\pi r/a_0) - 0.5)$ respectively. Each profile has been made dimensionless by rescaling by the initial core size a_0. **(B and E)** The percent error in $\Gamma \oint \vec{u} \cdot \vec{d\ell}$ relative to the helicity over time. **(C and F)** The core size over time for each initial state, normalized by the initial core size.

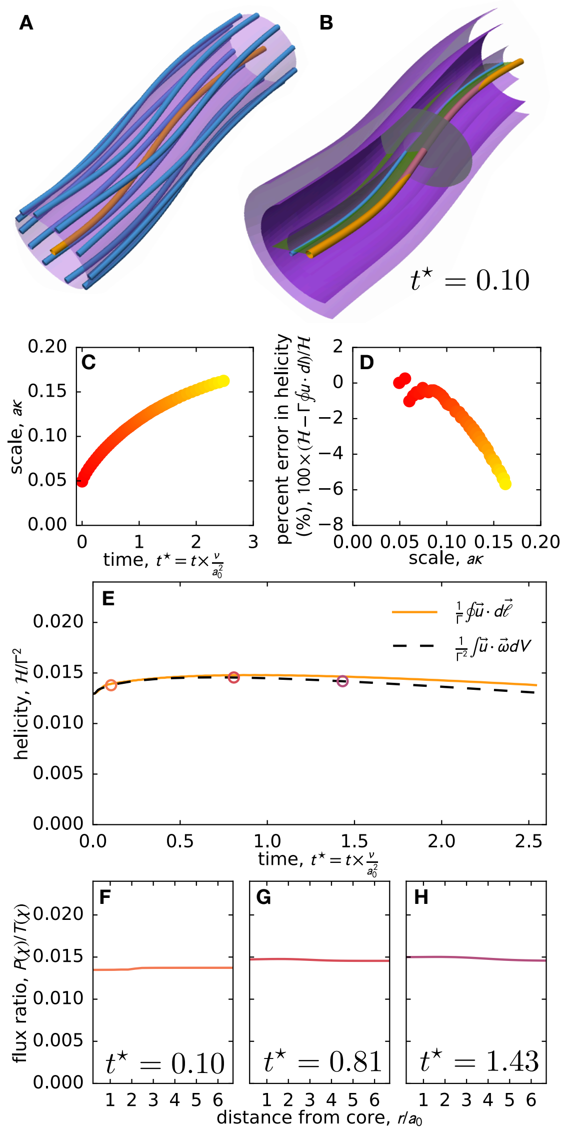

Figure 7: Simulation of a writhing vortex tube. **(A)** A vortex surface (purple) with vortex field-lines (cyan) nested about the center-line (gold). **(B)** Cutaways of vortex surfaces (purple) nested about the center-line (gold). The toroidal (gray) and poloidal (green) integration surfaces for a single vortex surface is shown, along with a vortex field-line that pierces each of them (cyan). **(C)** The dimensionless helicity of the volume over time compared to $\oint \vec{u} \cdot d\vec{\ell}/\Gamma$. **(D)** The scale of the vortex core over time. **(E)** The error in the center-line total helicity measurement relative to the scale of the core. **(F to H)** $P(\chi)/T(\chi)$ for various time steps.

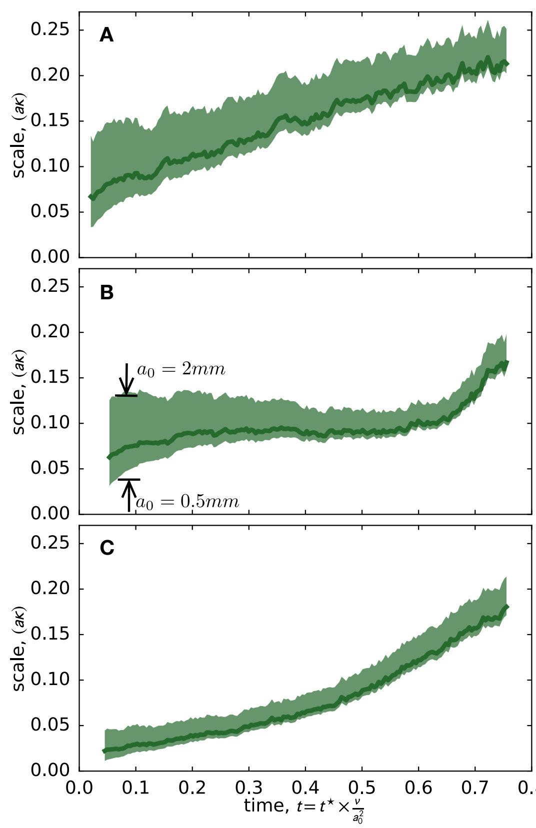

Figure 8: Estimated experimental separation of scale. **(A to C)** Estimated core scale for a typical isolated helix, stretched helix, and compressed helix respectively.

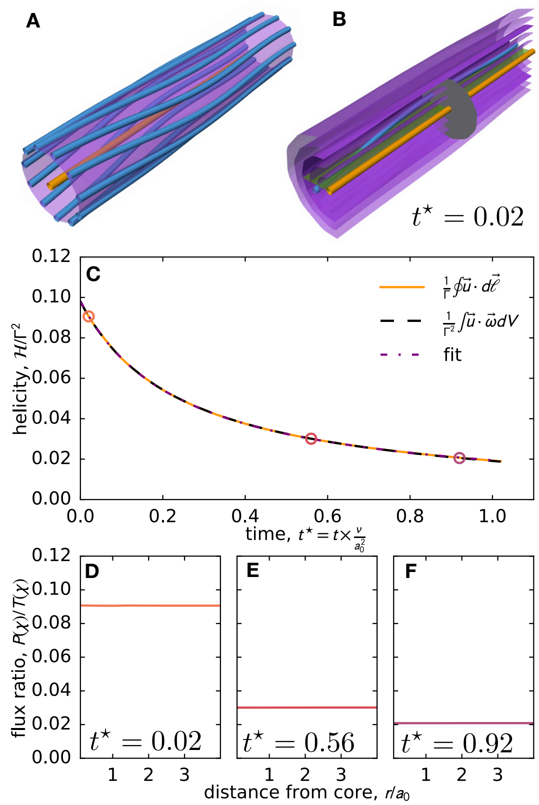

Figure 9: Measuring helicity with z-dependent twist. **(A)** A vortex surface (purple) with vortex field-lines (cyan) nested about the center-line (gold). **(B)** Cutaways of vortex surfaces (purple) nested about the center-line (gold). The toroidal (gray) and poloidal (green) integration surfaces for a single vortex surface as shown, along with a vortex field-line that pierces each of them (cyan). **(C)** The dimensionless helicity of the volume (dotted black line) over time compared to $\oint \vec{u}\cdot d\vec{\ell}/\Gamma$ (solid gold line). A profile of $f(t;a,b) = a/(bt+1)$ is fit to the helicity (dash-dotted purple line). **(D to F)** $P(\chi)/T(\chi)$ for various time steps.

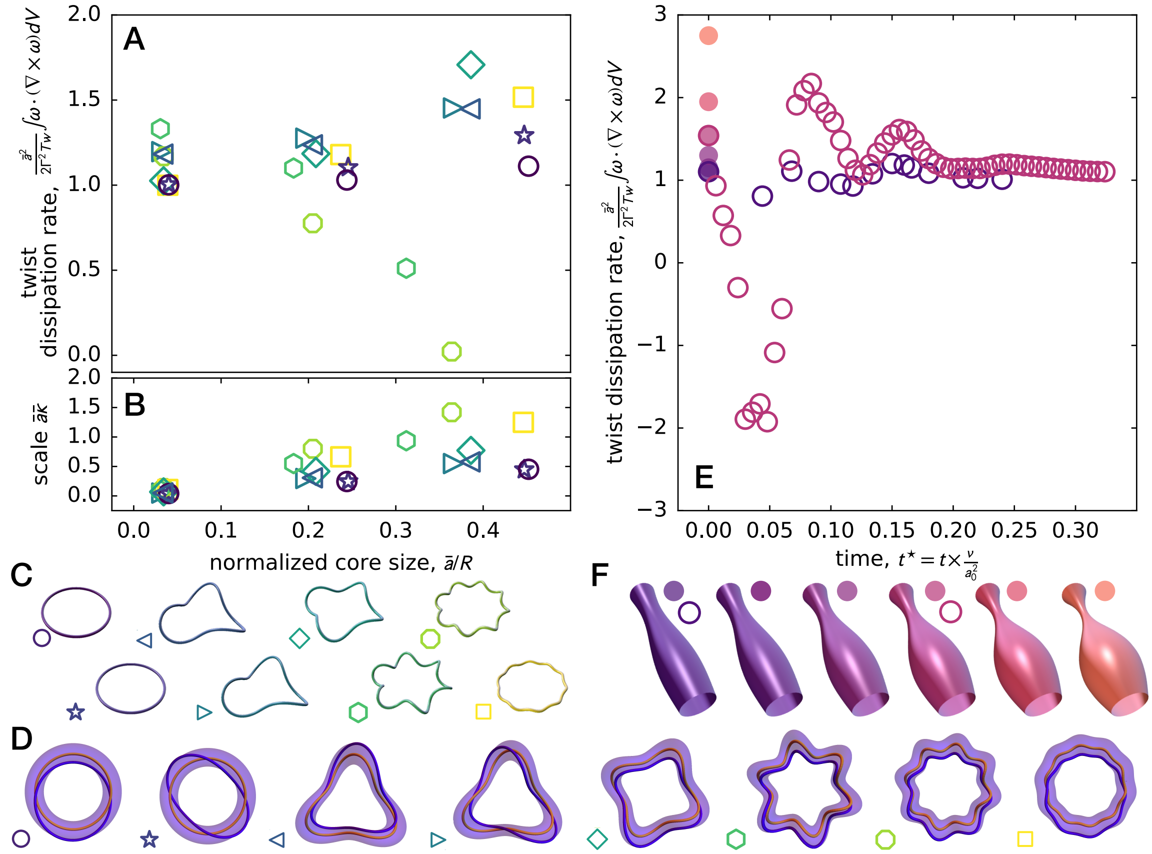

Figure 10: Twist dissipation rates for a variety of vortices. **(A)** The rate of change of helicity $\dot{\mathcal{H}}$ for a variety of vortex center-lines, normalized by $-4\nu/\bar{a}^2 \times \Gamma^2 Tw$, where $\bar{a}$ is the mean Gaussian width of the vorticity profile computed along the tube, and $Tw = \mathcal{H}/\Gamma^2 - Wr$ since there is no tube linking. Repeated shapes (ring, three-fold) have different total amounts of twist for the same center-line. **(B)** The scale of each tube, determined by $\bar{a}\bar{\kappa}$ where $\bar{\kappa}$ is the mean curvature of the center-line. **(C)** Glyphs showing the center-line geometry for each field considered in (A). **(D)** Vortex surfaces (transparent purple), center-lines (gold) and field-lines (solid purple) for shapes considered in (A). **(E)** The rate of change of helicity $\dot{\mathcal{H}}$ for straight line vortices with undulating Gaussian core profiles, given by $a(z) = a_0 + A\sin(2\pi z/L)$, normalized in the manner as in (A). The color indicates the degree of core profile modulation, beginning with $A = 0.25a_0$ (purple) and moving through $A = 0.3a_0$ to $A = 0.7a_0$ (light orange) in even steps of $0.1a_0$. Solid markers indicate computations performed on initial states, open markers show computations performed on states evolved according to the Navier-Stokes equations ($0.25a_0$ and $0.5a_0$ cases only) **(F)** Glyphs showing the value of $a(z)$ along each initial state considered in (E).

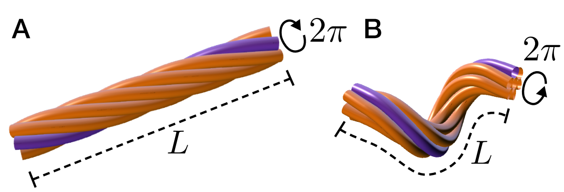

Figure 11: Straight and coiling twisted vortices. **(A)** A straight twisted vortex of length L where each filament winds by 2π around the center-line and the twist is $Tw = 1$. **(B)** A coiling twisted vortex also of length L and filaments winding 2π around the center-line where the twist is $Tw = 0.7$.

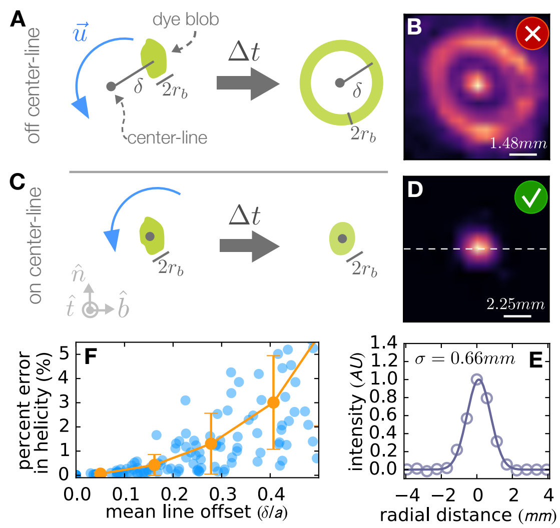

Figure 12: Center-line position verification. **(A)** A schematic showing the shearing of a dye blob offset from the center-line of the vortex, shown experimentally for dye purposefully seeded off the center-line in **(B)**. **(C)** Schematic showing the evolution of a dye blob placed on the center-line. **(D)** A cross-section of a typical blob used in each experiment. **(E)** The intensity sampled over the white line shown in (D). The solid curve is a Gaussian fit to the data. **(F)** The absolute percent difference between the correct helicity and the helicity measured using random paths with a variety of mean offsets from the center-line. The blue dots indicate the values for a random path, while the gold dots and their error bars are found by binning the data in units of $0.11a$ and then averaging the data and taking its standard deviation within each bin.

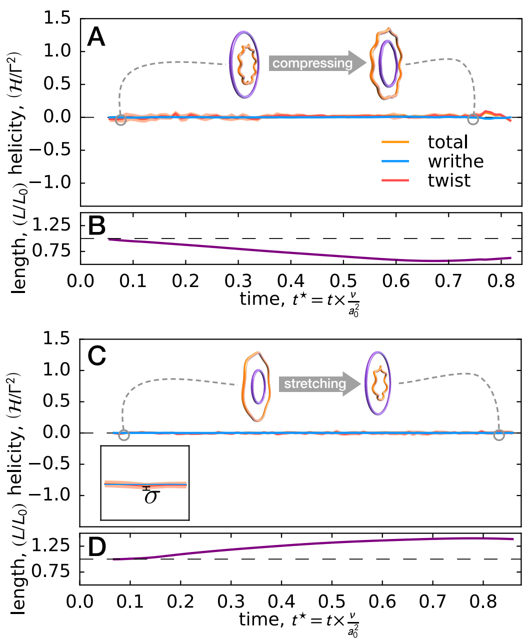

Figure 13: Helicity values of planar rings. **(A,B)** The helicity and length, respectively, of a planar ring as it compressed via leap-frogging with a helical ring. **(C,D)** The helicity and length, respectively, of a planar ring as it is stretched via leap-frogging with a helical ring. All times are rescaled by ν/a_0^2, where a_0 is taken to be $1.5mm$ in all cases.

Movie S1 Demonstration of topological equivalence between winding generated by linking, writhing, and twisting.

Movie S2 A stretched helix and compressed ring evolving in water. Vortex cores are seeded with dye blobs, whose paths are traced over time in warm colors and overlaid on the volume.

Movie S3 A compressed ring and stretched helix evolving in water. Vortex cores are seeded with dye blobs, whose paths are traced over time in warm colors and overlaid on the volume.

Movie S4 Vortex field lines of a simulated writhing vortex tube. Field lines are shown from canted-side and top-down perspectives. Each field line is colored by the value of $\vec{\omega} \cdot \vec{\nabla} \times \vec{\omega}$ at that point. Surface shows and isosurface of $|\vec{\omega}|^2$ equal to half the initial max value.

Movie S5 Helicity isosurfaces for a simulated writhing vortex tube. Surfaces are shown from canted-side and top-down perspectives, along with a cross-section of the helicity density in the xz plane.

Movie S6 Vortex field lines of a simulated straight twisted vortex tube. Field lines are shown from canted-side and top-down perspectives. Each field line is colored by the value of $\vec{\omega} \cdot \vec{\nabla} \times \vec{\omega}$ at that point. Surface shows and isosurface of $|\vec{\omega}|^2$ equal to half the initial max value.

Movie S7 Helicity isosurfaces for a straight twisted vortex tube. Surfaces are shown from canted-side and top-down perspectives, along with a cross-section of the helicity density in the xz plane.

References and Notes

1. H. K. Moffatt, The degree of knottedness of tangled vortex lines. *J. Fluid Mech.* **35**, 117–129 (1969). doi:10.1017/S0022112069000991

2. J. B. Taylor, Relaxation of toroidal plasma and generation of reverse magnetic fields. *Phys. Rev. Lett.* **33**, 1139–1141 (1974). doi:10.1103/PhysRevLett.33.1139

3. Y. Song, R. L. Lysak, Evaluation of twist helicity of flux transfer event flux tubes. *J. Geophys. Res. Space Physics* **94**, 5273–5281 (1989). doi:10.1029/JA094iA05p05273

4. M. A. Berger, Rigorous new limits on magnetic helicity dissipation in the solar corona. *Geophys. Astrophys. Fluid Dyn.* **30**, 79–104 (1984). doi:10.1080/03091928408210078

5. B. B. Kadomtsev, Disruptive instability in tokamaks. *Sov. J. Plasma Phys.* **1**, 710 (1975).

6. F. L. Waelbroeck, Current sheets and nonlinear growth of the m =1 kink-tearing mode. *Phys. Fluids B Plasma Phys.* **1**, 2372–2380 (1989). doi:10.1063/1.859172

7. H. K. Moffatt, A. Tsinober, Helicity in laminar and turbulent flow. *Annu. Rev. Fluid Mech.* **24**, 281–312 (1992). doi:10.1146/annurev.fl.24.010192.001433

8. H. Aref, I. Zawadzki, Linking of vortex rings. *Nature* **354**, 50–53 (1991). doi:10.1038/354050a0

9. H. K. Moffatt, Helicity and singular structures in fluid dynamics. *Proc. Natl. Acad. Sci. U.S.A.* **111**, 3663–3670 (2014). doi:10.1073/pnas.1400277111 Medline

10. C. E. Liang, R. L. Ricca, D. W. L. Sumners, Conservation of writhe helicity under anti-parallel reconnection. *Sci. Rep.* **5**, 9224 (2015). doi:10.1038/srep09224

11. S. Kida, M. Takaoka, Reconnection of vortex tubes. *Fluid Dyn. Res.* **3**, 257–261 (1988). doi:10.1016/0169-5983(88)90075-5

12. Y. Kimura, H. K. Moffatt, Reconnection of skewed vortices. *J. Fluid Mech.* **751**, 329–345 (2014). doi:10.1017/jfm.2014.233

13. M. V. Melander, F. Hussain, in *Center for Turbulence Research, Proceedings of the Summer Program 1988* (Center for Turbulence Research, 1988), pp. 257–286.

14. F. Maggioni, S. Alamri, C. F. Barenghi, R. L. Ricca, Velocity, energy, and helicity of vortex knots and unknots. *Phys. Rev. E Stat. Nonlin. Soft Matter Phys.* **82**, 026309 (2010). doi:10.1103/PhysRevE.82.026309 Medline

15. M. W. Scheeler, D. Kleckner, D. Proment, G. L. Kindlmann, W. T. M. Irvine, Helicity conservation by flow across scales in reconnecting vortex links and knots. *Proc. Natl. Acad. Sci. U.S.A.* **111**, 15350–15355 (2014). doi:10.1073/pnas.1407232111 Medline

16. R. L. Thompson, C. M. Mead, R. Edwards, Effective storm-relative helicity and bulk shear in supercell thunderstorm environments. *Weather Forecast.* **22**, 102–115 (2007). doi:10.1175/WAF969.1

17. D. K. Lilly, The structure, energetics and propagation of rotating convective storms. Part II: Helicity and storm stabilization. *J. Atmos. Sci.* **43**, 126–140 (1986). doi:10.1175/1520-0469(1986)043<0126:TSEAPO>2.0.CO;2

18. E. Levich, E. Tzvetkov, Helical cyclogenesis. *Phys. Lett. A* **100**, 53–56 (1984). doi:10.1016/0375-9601(84)90354-2

19. H. K. Moffatt, R. L. Ricca, Helicity and the Calugareanu invariant. *Proc. R. Soc. Lond. A* **439**, 411–429 (1992). doi:10.1098/rspa.1992.0159

20. R. H. Kraichnan, Helical turbulence and absolute equilibrium. *J. Fluid Mech.* **59**, 745–752 (1973). doi:10.1017/S0022112073001837

21. J. C. André, M. Lesieur, Influence of helicity on the evolution of isotropic turbulence at high Reynolds number. *J. Fluid Mech.* **81**, 187–207 (1977). doi:10.1017/S0022112077001979

22. P. R. Spalart, Airplane trailing vortices. *Annu. Rev. Fluid Mech.* **30**, 107–138 (1998). doi:10.1146/annurev.fluid.30.1.107

23. T. Gerz, F. Holzäpfel, D. Darracq, Commercial aircraft wake vortices. *Prog. Aerosp. Sci.* **38**, 181–208 (2002). doi:10.1016/S0376-0421(02)00004-0

24. C. P. Ellington, C. van den Berg, A. P. Willmott, A. L. R. Thomas, Leading-edge vortices in insect flight. *Nature* **384**, 626–630 (1996). doi:10.1038/384626a0

25. M. H. Dickinson, F.-O. Lehmann, S. P. Sane, Wing rotation and the aerodynamic basis of insect flight. *Science* **284**, 1954–1960 (1999). doi:10.1126/science.284.5422.1954 Medline

26. S. P. Sane, The aerodynamics of insect flight. *J. Exp. Biol.* **206**, 4191–4208 (2003). doi:10.1242/jeb.00663 Medline

27. H. K. Moffatt, S. Kida, K. Ohkitani, Stretched vortices – the sinews of turbulence; large-Reynolds-number asymptotics. *J. Fluid Mech.* **259**, 241 (1994). doi:10.1017/S002211209400011X

28. S. Douady, Y. Couder, M. E. Brachet, Direct observation of the intermittency of intense vorticity filaments in turbulence. *Phys. Rev. Lett.* **67**, 983–986 (1991). doi:10.1103/PhysRevLett.67.983 Medline

29. U. Frisch, A. N. Kolmogorov, *Turbulence: The Legacy of A. N. Kolmogorov* (Cambridge Univ. Press, 1995).

30. M. V. Berry, Quantal phase factors accompanying adiabatic changes. *Proc. R. Soc. Lond. A* **392**, 45–57 (1984). doi:10.1098/rspa.1984.0023

31. R. Y. Chiao, Y.-S. Wu, Manifestations of Berry's topological phase for the photon. *Phys. Rev. Lett.* **57**, 933–936 (1986). doi:10.1103/PhysRevLett.57.933 Medline

32. S. Pancharatnam, Generalized theory of interference, and its applications. Part I. Coherent pencils. *Proc. Indian Acad. Sci. A* **44**, 247–262 (1956).

33. A. Tomita, R. Y. Chiao, Observation of Berry's topological phase by use of an optical fiber. *Phys. Rev. Lett.* **57**, 937–940 (1986). doi:10.1103/PhysRevLett.57.937 Medline

34. M. A. Berger, G. B. Field, The topological properties of magnetic helicity. *J. Fluid Mech.* **147**, 133–148 (1984). doi:10.1017/S0022112084002019

35. Details are given in the supplementary text (Calculation of total helicity).

36. Details are given in the materials and methods (Tracer identification, tracking, and analysis protocol).

37. Details are given in the materials and methods (Hydrofoil shapes and specifications).

38. D. Kleckner, W. T. M. Irvine, Creation and dynamics of knotted vortices. *Nat. Phys.* **9**, 253–258 (2013). doi:10.1038/nphys2560

39. W. Thielicke, E. Stamhuis, PIVlab – Towards user-friendly, affordable and accurate digital particle image velocimetry in MATLAB. *J. Open Res. Softw.* **2**, e30 (2014). doi:10.5334/jors.bl

40. Details are given in the materials and methods (Measuring circulation via PIV).

41. Details are given in the supplementary text (Helicity values of planar loops).

42. H. Pfister, W. Gekelman, Demonstration of helicity conservation during magnetic reconnection using Christmas ribbons. *Am. J. Phys.* **59**, 497–502 (1991). doi:10.1119/1.16808

43. Details are given in the supplementary text (Estimating dissipation with dimensional analysis).

44. D. Kleckner, L. H. Kauffman, W. T. M. Irvine, How superfluid vortex knots untie. *Nat. Phys.* **12**, 650–655 (2016). doi:10.1038/nphys3679

45. G. L. Kindlmann, R. San José Estépar, S. M. Smith, C. F. Westin, Sampling and visualizing creases with scale-space particles. *IEEE Trans. Vis. Comput. Graph.* **15**, 1415–1424 (2009). doi:10.1109/TVCG.2009.177 Medline

46. J. A. Sethian, A fast marching level set method for monotonically advancing fronts. *Proc. Natl. Acad. Sci. U.S.A.* **93**, 1591–1595 (1996). doi:10.1073/pnas.93.4.1591 Medline

47. D. B. Allan, T. A. Caswell, N. C. Keim, Trackpy v0.2 (2014); https://zenodo.org/record/9971.

48. P. Koumoutsakos, A. Leonard, High-resolution simulations of the flow around an impulsively started cylinder using vortex methods. *J. Fluid Mech.* **296**, 1 (1995). doi:10.1017/S0022112095002059

49. G.-H. Cottet, P. Koumoutsakos, *Vortex Methods, Theory and Practice* (Cambridge Univ. Press, 2000).

50. I. Sbalzarini, J. H. Walther, M. Bergdorf, S. E. Hieber, E. M. Kotsalis, P. Koumoutsakos, PPM – A highly efficient parallel particle–mesh library for the simulation of continuum systems. *J. Comput. Phys.* **215**, 566–588 (2006). doi:10.1016/j.jcp.2005.11.017

51. W. M. van Rees, A. Leonard, D. Pullin, P. Koumoutsakos, A comparison of vortex and pseudo-spectral methods for the simulation of periodic vortical flows at high Reynolds numbers. *J. Comput. Phys.* **230**, 2794–2805 (2011). doi:10.1016/j.jcp.2010.11.031

52. R. W. Hockney, J. W. Eastwood, *Computer Simulation Using Particles* (McGraw-Hill, 1981).

53. P. Chatelain, P. Koumoutsakos, A Fourier-based elliptic solver for vortical flows with periodic and unbounded directions. *J. Comput. Phys.* **229**, 2425–2431 (2010). doi:10.1016/j.jcp.2009.12.035

54. M. Pippig, PFFT: An extension of FFTW to massively parallel architectures. *SIAM J. Sci. Comput.* **35**, C213–C236 (2013). doi:10.1137/120885887

55. G. Călugăreanu, Sur les classes d'isotopie des noeuds tridimensionnels et leurs invariants. *Czech. Math. J.* **11**, 588 (1961).

56. J. H. White, Self-linking and the Gauss integral in higher dimensions. *Am. J. Math.* **91**, 693 (1969). doi:10.2307/2373348

57. F. B. Fuller, The writhing number of a space curve. *Proc. Natl. Acad. Sci. U.S.A.* **68**, 815–819 (1971). doi:10.1073/pnas.68.4.815 Medline

58. A. Y. K. Chui, H. K. Moffatt, The energy and helicity of knotted magnetic flux tubes. *Proc. R. Soc. Lond. A* **451**, 609–629 (1995). doi:10.1098/rspa.1995.0146

59. H. Kedia, D. Foster, M. R. Dennis, W. T. Irvine, Weaving knotted vector fields with tunable helicity. *Phys. Rev. Lett.* **117**, 274501 (2016). doi:10.1103/PhysRevLett.117.274501 Medline

60. R. Littlejohn, Singular Poisson tensors. *AIP Conf. Proc.* **88**, 47 (1982).